npj computational materials

www.nature.com/npjcompumats

ARTICLE OPEN

Check for updates

Exploitable magnetic anisotropy and half-metallicity controls in multiferroic van der Waals heterostructure

Yaping Wang[1], Xinguang Xu[1], Weixiao Ji[2], Shengshi Li[2]✉, Yanlu Li[1]✉ and Xian Zhao[3]✉

Two-dimensional (2D) XY ferromagnets have drawn pronounced interest in recent years, but the characteristic of easy-plane magnetization restricts their application in spintronics to some extent. Here, we propose a general strategy for constructing multiferroic van der Waals heterostructures, aiming to achieve electrical control over the magnetic anisotropy in 2D XY ferromagnets. The validity of this strategy is verified by the heterostructure composed of ferromagnetic VBi_2Te_4 and ferroelectric In_2Se_3 monolayers. By manipulating the polarized states of In_2Se_3, the VBi_2Te_4 can be reversibly transformed between 2D XY and Heisenberg ferromagnets, characterized by the switching of easy magnetization axis between in-plane and out-of-plane directions. More interestingly, accompanied by the changes in magnetic anisotropy, the VBi_2Te_4 also demonstrates a phase transition from a semiconductor to a half-metal state, which can be ascribed to the band alignment and interfacial charge transfer. The switchable magnetic and electronic properties enable the heterostructure to be utilized in nonvolatile memory and logic devices. Additionally, the half-metallicity and magnetocrystalline anisotropy energy of the heterostructure can be effectively tuned by biaxial strain. These findings not only pave the way for electrically nonvolatile control of 2D XY ferromagnet, but also facilitate the development of interfacial magnetoelectric physics and applications.

npj Computational Materials (2023)9:223 ; https://doi.org/10.1038/s41524-023-01178-2

INTRODUCTION

The discovery of ferromagnetism in two-dimensional (2D) ultrathin crystals[1–4] has attracted prodigious research interest in recent years since it provides a remarkable opportunity to explore intriguing physical phenomena and develop innovative spintronic devices. Currently, most of the attention has been focused on 2D ferromagnets with perpendicular magnetic anisotropy (PMA), such as CrI_3 (Ising ferromagnet) and $Cr_2Ge_2Te_6$ (Heisenberg ferromagnet)[5–8], whose long-range ferromagnetic (FM) ordering can be observed experimentally. In fact, certain progress has also been achieved in experimental studies on 2D XY ferromagnets, which are characterized by easy-plane magnetization[9–13]. Nevertheless, the easy-plane magnetization is susceptible to thermal fluctuations, thereby prohibiting long-range FM ordering at any finite temperature according to the Mermin-Wagner theorem[14], which partially restricts the application of 2D XY ferromagnets in spintronics. In this scenario, the realization of switching the easy magnetization axis from in-plane to out-of-plane directions in a 2D XY ferromagnet holds significant implications for both fundamental research and practical applications.

Various approaches have been proposed up till now to achieve this goal[15–19], with the purely electrical control of magnetic anisotropy being the most desirable due to its compatibility with the development requirements of next-generation magnetic storage technology. It has been reported that by increasing the electric field, the easy magnetization axis of the VSi_2P_4 monolayer can be switched from in-plane to out-of-plane directions[15], suggesting the possibility of electrically controlled magnetic anisotropy in 2D XY ferromagnets. However, the volatility in the manipulation of magnetic anisotropy remains a fundamental question that needs to be resolved. In other words, maintaining the induced state requires a persistent electric field, which will inevitably result in increased energy consumption. This presents a significant challenge to the advancement of energy-efficient memory and logic devices.

With the successful fabrication of 2D ferroelectrics[20–25], constructing multiferroic van der Waals (vdW) heterostructures based on 2D magnets and ferroelectrics provides a practicable strategy for addressing the aforementioned confusion. The ideal magnetoelectric coupling in heterostructures enables the magnetic behavior in magnets to be tailored by reversing the electric polarization of ferroelectrics. More importantly, considering that the spontaneous polarization of ferroelectric is retained even when the externally applied electric field is removed, nonvolatile electrical control of magnetism is accessible in multiferroic vdW heterostructures. To date, the nonvolatile tuning of magnetic ordering and phase transition between half-metal and semiconductor via switching the ferroelectric polarization have been predicted in diverse multiferroic vdW heterostructures, including CrI_3/Sc_2CO_2[26], CrI_3/In_2Se_3[27], FeI_2/In_2Se_3[28], NiI_2/In_2Se_3[29], and Sc_2CO_2/VSe_2[30]. In view of this, we propose a scheme that aims to realize the transition of the easy magnetization axis from in-plane to out-of-plane directions in a 2D XY ferromagnets by designing a multiferroic vdW heterostructure, as illustrated in Fig. 1. Owing to the broken spatial inversion symmetry in the ferroelectric substrate, polarization flipping holds promise for inducing atomic orbital redistribution in the XY ferromagnet, which makes possible the electrically controlled alteration of magnetic anisotropy. Accordingly, the switching on-off of long-range FM ordering and the transformation between 2D XY and Heisenberg ferromagnets become achievable. Beyond that, as the polarization of the ferroelectric is reversed, different interfaces can be obtained in the heterostructure, leading to distinct band alignment and interfacial charge transfer. This provides an

[1]State Key Lab of Crystal Materials and Institute of Crystal Materials, Shandong University, Jinan 250100, China. [2]Spintronics Institute, University of Jinan, Jinan 250022, China. [3]Center for Optics Research and Engineering of Shandong University, Shandong University, Qingdao 266237, China. ✉email: sdy_liss@ujn.edu.cn; liyanlu@sdu.edu.cn; xianzhao@sdu.edu.cn

opportunity to realize the conversion between half-metal (or metal) and semiconductor states for the 2D ferromagnet while tuning the easy magnetization axis. If realized, both the polarization direction of the ferroelectric and the magnetic anisotropy of the ferromagnet can be directly detected by electrical signals, which would greatly benefit data reading processes in storage devices.

Recently, the 2D VBi_2Te_4 monolayer has been predicted as a member of the $MnBi_2Te_4$-family materials[31]. The favorable dynamical stability of the VBi_2Te_4 monolayer suggests that it can possibly be synthesized through experiments. Different from the $MnBi_2Te_4$ monolayer, which has an out-of-plane easy magnetization axis, the VBi_2Te_4 monolayer exhibits the easy-plane magnetization characteristic of a typical 2D XY ferromagnet[31–33]. To validate our conception, we propose a multiferroic vdW heterostructure composed of FM VBi_2Te_4 and ferroelectric In_2Se_3 monolayers. As the electric polarization of the In_2Se_3 is reversed from upward to downward, the VBi_2Te_4 undergoes a transition from 2D XY to Heisenberg ferromagnets, featured by the switching of the easy magnetization axis from in-plane to out-of-plane directions. The Curie temperature (T_C) of the VBi_2Te_4 monolayer, which behaves as a Heisenberg ferromagnet, is evaluated to be 76 K based on Monte Carlo (MC) simulation. In addition to the tuning of magnetic anisotropy, electrically controlled transformation from a semiconductor to a half-metal state is also achieved for the VBi_2Te_4 monolayer, which can be comprehended by band alignment and interfacial charge transfer. Based on the multiferroic vdW heterostructure, a conceptual memory device for high-density data storage is designed. The half-metallic property and magnetocrystalline anisotropy energy (MAE) of the VBi_2Te_4 monolayer in the heterostructure are also tunable by strain engineering. Our achieved results provide promising platforms for the exploration of advanced spintronic devices.

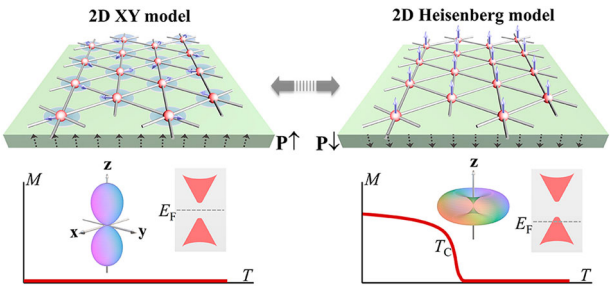

Fig. 1 Schematic representation of transition between 2D XY and Heisenberg models. The upper panels depict the reversal of the easy magnetization axis induced by polarization flipping, while the lower panels illustrate the magnetic anisotropy, Curie temperature, and electronic properties for 2D XY and Heisenberg models, respectively.

RESULTS AND DISCUSSION

VBi_2Te_4/In_2Se_3 heterostructure

Let us commence with the fundamental properties of individual VBi_2Te_4 and In_2Se_3 monolayers. The VBi_2Te_4 monolayer crystallizes in the $R\bar{3}m$ space group with a triangular lattice, as demonstrated in Fig. 2a, and its optimized lattice constant is 4.36 Å. The calculated phonon dispersions presented in Supplementary Fig. 1 indicate that the VBi_2Te_4 monolayer is dynamically stable, as no imaginary modes are observed across the entire Brillouin zone. The magnetic ground state of the VBi_2Te_4 monolayer is determined by constructing both FM and antiferromagnetic (AFM) configurations, as shown in Supplementary Fig. 2. Based on the relative energy of these magnetic configurations listed in Supplementary Table 1, it is found that the VBi_2Te_4 monolayer prefers FM coupling with a magnetic moment of 3.0 μ_B per V atom. The MAE of the VBi_2Te_4 monolayer is also calculated, which is defined as the energy difference between the spin moments along the in-plane and out-of-plane directions, namely, $E_{MAE} = E_{in\text{-}plane} - E_{out\text{-}of\text{-}plane}$. The E_{MAE} is found to be −0.24 meV per unit cell, which closely agrees with previously reported values[31,33], revealing that the VBi_2Te_4 monolayer is a 2D XY ferromagnet. Supplementary Fig. 3a presents the band structure of the VBi_2Te_4 monolayer, in which a semiconducting nature with an indirect band gap of 0.93 eV can be observed. On the other hand, the free-standing In_2Se_3 monolayer exhibits a hexagonal structure with a lattice constant of 4.10 Å, see Fig. 2b. Our calculations predict an out-of-plane polarization of 0.16×10^{-10} C m^{-1} for this monolayer. According to the band structure presented in Supplementary Fig. 3b, the In_2Se_3 monolayer behaves as a semiconductor with an indirect band gap of 0.78 eV. All these results are consistent with previous calculations[34,35].

The multiferroic vdW heterostructure is then constructed by vertically stacking the VBi_2Te_4 monolayer on the In_2Se_3 monolayer, denoted as VBi_2Te_4/In_2Se_3. Here, the lattice constant of the VBi_2Te_4 monolayer remains fixed in the heterostructure to preserve its physical properties and minimize strain-induced alterations, while the In_2Se_3 monolayer is stretched by 5.73% to match that of the VBi_2Te_4. Despite being stretched, the semiconducting nature of

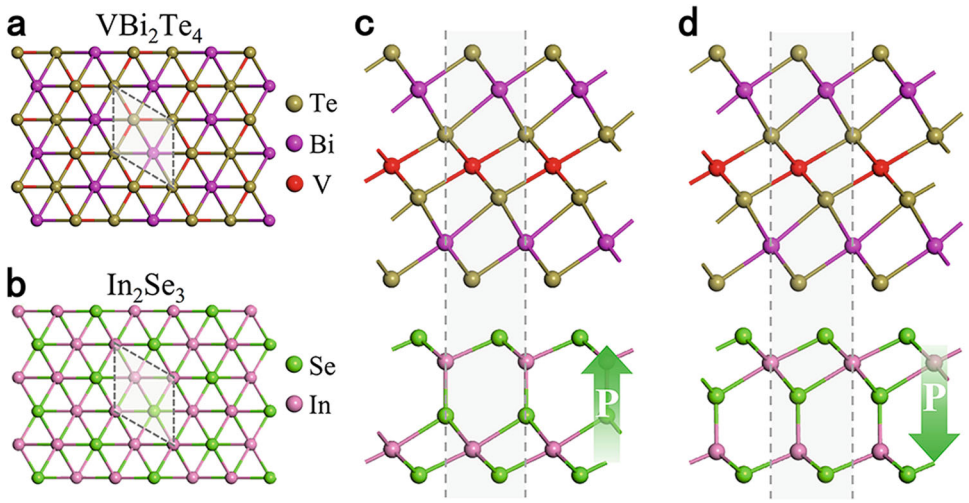

Fig. 2 Geometric structures of free-standing monolayers and heterostructures. a, **b** Top views of 2D VBi_2Te_4 and In_2Se_3 monolayers. **c**, **d** Side views of optimal configuration for the VBi_2Te_4/In_2Se_3 heterostructure with P↑ and P↓ states.

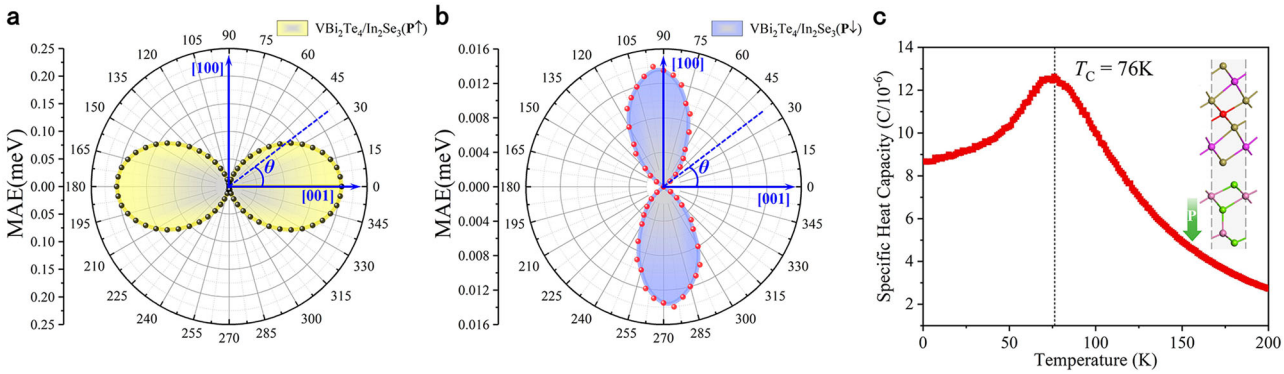

Fig. 3 Magnetic properties of the VBi_2Te_4/In_2Se_3. a, **b** Dependence of the MAE on the polar angle θ for the VBi_2Te_4/In_2Se_3 heterostructure in P↑ and P↓ configurations. **c** Simulated specific heat C_V in terms of the temperature for the VBi_2Te_4/In_2Se_3 heterostructure with the P↓ state.

the In_2Se_3 monolayer is maintained, with a decreased band gap of 0.34 eV and a shifted valence band maximum (VBM) to the K point, as illustrated in Supplementary Fig. 3c. Meanwhile, the magnitude of out-of-plane polarization for the stretched In_2Se_3 monolayer is also decreased to 0.10×10^{-10} C m^{-1}. Since the In_2Se_3 monolayer possesses two bistable polarization states, the heterostructure has two polarization configurations (i.e., P↑ and P↓). To determine the optimal geometric structure of P↑ and P↓ configurations, six highly-symmetric stacking patterns between VBi_2Te_4 and In_2Se_3 are taken into account, as illustrated in Supplementary Fig. 4. According to the relative energy listed in Supplementary Table 2, we find that the Dn-I and Up-I configurations, with the V atom located above the lower In atom, are the most robust, see Fig. 2c, d. Further research studies will be conducted on these two configurations in the following sections. After structural relaxation, the optimized interlayer distances are found to be 2.66 and 2.47 Å for P↑ and P↓ configurations, respectively. Notably, the minimum atomic distance (Te-Se) at the interface is approximately 3.60 Å, which is much larger than the sum of their covalent radii, suggesting that the interlayer coupling is chiefly governed by vdW interactions. The binding energy (E_b) of the VBi_2Te_4/In_2Se_3 heterostructure is also evaluated using the formula of $E_b = (E_{VBi_2Te_4/In_2Se_3} - E_{VBi_2Te_4} - E_{In_2Se_3})/S$. Here, $E_{VBi_2Te_4/In_2Se_3}$ is the total energy of VBi_2Te_4/In_2Se_3, while $E_{VBi_2Te_4}$ and $E_{In_2Se_3}$ represent the energies of individual VBi_2Te_4 and In_2Se_3 monolayers, respectively, and S refers to the surface area. The resultant E_b is about −0.20 eV Å^{-2}, indicating that the VBi_2Te_4/In_2Se_3 is a vdW heterostructure, and the negative value implies that the heterostructure is energetically stable and promising for experimental fabrication. Besides, the feasibility of ferroelectricity in the VBi_2Te_4/In_2Se_3 heterostructure is explored. The transition path from P↑ to P↓ states is illustrated in Supplementary Fig. 5, which involves passing through a paraelectric state. The energy barrier for this path is found to be 0.47 eV per unit cell, indicating the potential accessibility of ferroelectricity in the heterostructure.

Next, we put our emphasis on the magnetic properties of the VBi_2Te_4/In_2Se_3. We first examine the magnetic ground state of the VBi_2Te_4 monolayer in the heterostructure. Similar to the free-standing VBi_2Te_4 monolayer, both FM and AFM states are considered for P↑ and P↓ configurations, as illustrated in Supplementary Fig. 2. The relative energies of different magnetic states are listed in Supplementary Table 1, where it is observed that the FM state is energetically lower than the AFM states, revealing that the VBi_2Te_4 monolayer retains its original FM ground state. The response of magnetic anisotropy in the VBi_2Te_4 monolayer to polarization switching of the In_2Se_3 monolayer is also studied. Figure 3a, b presents the dependence of the MAE on the polar angle (θ) for P↑ and P↓ configurations. It shows that in the P↑configuration, the 2D VBi_2Te_4 maintains its easy-plane magnetization characteristic, and the E_{MAE} decreases to −0.20 meV per unit cell due to the proximity effect. Intriguingly, for the P↓ configurations, the easy magnetization axis of the VBi_2Te_4 monolayer is switched to the out-of-plane direction, along with a E_{MAE} of 0.01 meV per unit cell. The presence of PMA can overcome the Mermin-Wagner constraint and counteract thermal fluctuations, thereby giving rise to long-range FM ordering in the VBi_2Te_4 monolayer. In other words, the polarization flipping of the In_2Se_3 monolayer is capable of driving the 2D VBi_2Te_4 to experience a transition between 2D XY and Heisenberg ferromagnets (i.e., switching on-off of the long-range FM ordering). It also confirms that the VBi_2Te_4/In_2Se_3 heterostructure harbors a strong magnetoelectric coupling effect, enabling the nonvolatile electrical control of magnetic anisotropy in the VBi_2Te_4 monolayer.

In the heterostructure with the P↓ state, the VBi_2Te_4 monolayer transforms into a 2D Heisenberg ferromagnet. The key parameter T_C is therefore evaluated through MC simulation. Here, considering the disruption of spatial inversion symmetry in the VBi_2Te_4 monolayer caused by the ferroelectric polarization of the In_2Se_3 monolayer, we incorporate the Dzyaloshinskii-Moriya interaction (DMI). The model Hamiltonian can be described as:

$$H = -J_1\sum_{i,j} S_i \cdot S_j - J_2\sum_{k,l} S_k \cdot S_l - J_3\sum_{m,n} S_m \cdot S_n - K\sum_i (S_i^z)^2 - D\sum_{i,j}(S_i \times S_j). \quad (1)$$

Here, J_1, J_2, and J_3 are the nearest, next-nearest-, and next-next-nearest-neighbor exchange coupling parameters, respectively; $\mathbf{S}_i$ denotes the spin vector at the i-th V site; S_i^z represents the spin component parallel to the z direction; K is the single-ion anisotropy and $\mathbf{D}$ is the DM vector. The detailed calculations for J_1, J_2, J_3, K, and $\mathbf{D}$ are available in Appendix I of the Supplementary Material. In MC simulation, a 100×100×1 supercell with periodic boundary conditions is adopted, and a total of 1×10^6 MC steps are employed for each temperature point. The value of T_C can be determined by locating the peak position in the specific heat C_V curve, while the specific heat capacity is evaluated by $C_v = \frac{(\langle E^2\rangle - \langle E\rangle^2)}{k_B T^2}$. Figure 3c displays the simulated C_V curve, and the T_C is predicted to be 76 K, which is higher than that of previously reported 2D ferromagnets, e.g., CrI_3 (45 K)[1], $CrBr_3$ (34 K)[36], and $CrGeTe_3$ (30 K)[2]. Therefore, the introduction of the ferroelectric In_2Se_3 monolayer enhances the potential applications of the VBi_2Te_4 monolayer in spintronics.

The influence of the ferroelectric proximity effect on the electronic properties of the VBi_2Te_4 monolayer is then explored. The band structures of two polarization configurations are shown in Fig. 4a, b. For the P↑ case, a semiconducting nature is obtained with an indirect band gap of 0.52 eV. The VBM and conduction band minimum (CBM) are essentially governed by the monolayers of VBi_2Te_4 and In_2Se_3, respectively, resulting in a type-II band alignment (see Fig. 4a). According to the density of states (DOS) in

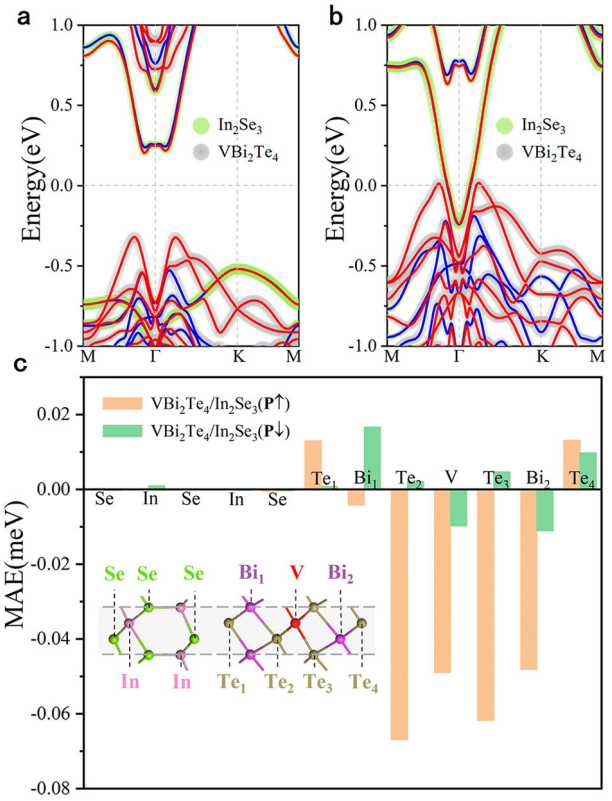

Fig. 4 Electronic properties and MAE contribution of the VBi_2Te_4/In_2Se_3. **a**, **b** Calculated band structures of the VBi_2Te_4/In_2Se_3 heterostructure with P↑ and P↓ states. The red and blue lines represent the spin-up and spin-down states, respectively. **c** Atom-resolved MAE of the VBi_2Te_4/In_2Se_3 heterostructure with P↑ and P↓ states.

Supplementary Fig. 7a, the VBM mainly originates from the $V-d_{z^2}$ orbital, while the CBM is contributed by the In-*s* and Se-$p_{x,y}$ orbitals. It is also noteworthy that the lowest conduction band shows a slight spin splitting, indicating that the In_2Se_3 monolayer becomes magnetized due to the magnetic proximity effect. When the polarization of the In_2Se_3 monolayer is switched to the P↓ state, the Fermi level intersects with the energy bands, leading to hole and electron pockets for VBi_2Te_4 and In_2Se_3, respectively (see Fig. 4b). More interestingly, at the Fermi level, the energy band stemming from the VBi_2Te_4 monolayer is completely dominated by the spin-up state. Due to the spatial separation of hole and electron pockets, the VBi_2Te_4 monolayer exhibits a half-metallic property, whereas the In_2Se_3 monolayer displays metallic behavior, as shown in Supplementary Fig. 7b. Therefore, reversing the polarization of the In_2Se_3 monolayer from upward to downward can induce a transition from a semiconductor to a half-metal for the 2D VBi_2Te_4. When considering the spin-orbit coupling (SOC) effect, it is observed that neither the electronic properties of P↑nor those of P↓ configurations undergo a significant change in nature, except for a decrease in band gap for the former, as illustrated in Supplementary Fig. 8. The phase transition from a semiconductor to a half-metal is also well preserved in the VBi_2Te_4 monolayer. While previous studies have demonstrated the feasibility of individually controlling half-metallicity or magnetic anisotropy in multiferroic heterostructures, such as CrI_3/Sc_2CO_2[26], $MnCl_3/CuInP_2S_6$[37], $Cr_2Ge_2Te_6/Sc_2CO_2$[38], and $Cr_2Ge_2Te_6/In_2Se_3$[39], our VBi_2Te_4/In_2Se_3 heterostructure offers a particular opportunity for simultaneous control over both half-metallicity and magnetic anisotropy. The realization of multidimensional regulation within this heterostructure will significantly enhance the functionality of electronic devices. Considering that the VBi_2Te_4 and $MnBi_2Te_4$ monolayers belong to the same material family, we have also constructed the $MnBi_2Te_4/In_2Se_3$ multiferroic heterostructure to validate the possibility of magnetoelectric coupling effect. As shown in Supplementary Fig. 9, the $MnBi_2Te_4$ monolayer solely exhibits an electrically controlled phase transition from a semiconductor to a half-metal, whereas its PMA remains unaffected by the polarization switching of the In_2Se_3 monolayer, which is consistent with previous research findings[40].

Having established the nonvolatile electrical control of magnetic and electronic properties in the VBi_2Te_4/In_2Se_3 heterostructure, our focus now shifts to elucidating the origin of MAE in this heterostructure. Figure 4c illustrates the atom-resolved MAE of two polarization configurations. It is evident that the VBi_2Te_4 monolayer primarily contributes to the MAE, while the contribution of the In_2Se_3 monolayer is almost negligible. For the P↑ configuration, the Te_1 and Te_4 atoms contribute to the PMA, whereas the Te_2, Bi_1, V, Bi_2, and Te_3 atoms are responsible for the in-plane magnetic anisotropy (IMA). It should be noted that the contribution of the latter is remarkably larger than that of the former, resulting in easy-plane magnetization for the VBi_2Te_4 monolayer in the heterostructure. As the In_2Se_3 monolayer is switched to the P↓ state, a sign reversal occurs in the MAE contribution from Bi_1, Te_2, and Te_3 atoms. Accompanied by a significant decrease in MAE contribution from V and Bi_2 atoms, the overall MAE contribution becomes positive, indicating that the VBi_2Te_4 monolayer exhibits the PMA. Therefore, the sign change in MAE for Bi_1, Te_2, and Te_3 atoms plays a decisive role in the transition of magnetic anisotropy in the VBi_2Te_4 monolayer. To further elucidate this point, we calculate the orbital-resolved MAE of these atoms in the heterostructure with different polarized states, see Supplementary Fig. 10. In the P↑ configuration, the MAE contribution from the Bi_1 atom arises from the hybridizations between p_x and p_y orbitals, as well as between p_y and p_z orbitals, which exhibit positive and negative values, respectively. Obviously, the magnitude of the former is smaller than that of the latter, thereby establishing the contribution of the Bi_1 atom to the IMA. However, for Te_2 and Te_3 atoms, the hybridization between p_x and p_y orbitals contribute to the IMA, while that between p_y and p_z orbitals contribute to the PMA. The contribution from the former is predominant, ultimately leading to the overall IMA. When the ferroelectric polarization of the In_2Se_3 monolayer is reversed, the MAE contribution from the Bi_1 atom is determined by the hybridizations between p_x and p_y orbitals, as well as between p_x and p_z orbitals. Both contributions are positive, implying that the Bi_1 atom contributes to the PMA. Besides, the signs of hybridizations between p_x and p_y orbitals, as well as between p_x and p_z orbitals, for both Te_2 and Te_3 atoms are reversed accordingly. The MAE are dominated by the former, which provides a positive contribution. Hence, both Te_2 and Te_3 atoms also exhibits the PMA contribution.

Furthermore, we qualitatively interpret the ferroelectricity-dependent magnetic anisotropy in the VBi_2Te_4/In_2Se_3 heterostructure based on second-order perturbation theory[41,42]. According to the theory, the MAE can be expressed as:

$$MAE = \sum_{\sigma\sigma'} E^{\sigma\sigma'}(x) - E^{\sigma\sigma'}(z) = \sum_{\sigma\sigma'}(2\delta_{\sigma\sigma'} - 1)\xi^2 \sum_{o^\sigma u^{\sigma'}} \frac{|o^\sigma|L_z|u^{\sigma'}|^2 - |o^\sigma|L_x|u^{\sigma'}|^2}{E_u^{\sigma'} - E_o^\sigma} \quad (2)$$

where ξ represents the SOC amplitude, while $E_u^{\sigma'}$ and E_o^σ are the energy levels of unoccupied states with spin σ′ and occupied states with spin σ, respectively. $(2\delta_{\sigma\sigma'} - 1)(|o^\sigma|L_z|u^{\sigma'}|^2 - |o^\sigma|L_x|u^{\sigma'}|^2)$ is the difference of spin-orbital angular momentum matrix elements, which is shown in Supplementary Table 3. The equation suggests that the MAE is primarily determined by the matrix element differences and energy differences. In particular, the electronic states near the Fermi

level play a dominant role in contributing to the MAE due to their small energy separation ($E_u^{\sigma\prime} - E_o^{\sigma}$) in the denominator of the equation. Additionally, the total MAE may also be affected by the intensity of DOS as it is the integral of all occupied and unoccupied states[42–44]. Supplementary Fig. 11 shows the projected DOS of p orbitals for Bi_1, Te_2, and Te_3 atoms in the VBi_2Te_4/In_2Se_3 heterostructure with opposite polarizations. In the P↑ configuration, for the Bi_1 atom, the main occupied and unoccupied states near the Fermi level are governed by the spin-up state, see Supplementary Fig. 11a. This indicates that the SOC-induced total energy changes are determined by the hybridization between spin-up occupied and unoccupied states. Supplementary Table 3 lists the matrix element differences between spin-up occupied and unoccupied p states (p^{o+} and p^{u+}) in Eq. (2). From Supplementary Fig. 11a, one can observe that the main occupied states near the Fermi level originate from degenerate spin-up p_x and p_y states (p_x^{o+} and p_y^{o+}). Based on the data in Supplementary Table 3, the contribution to MAE can be obtained from hybridizations between spin-up unoccupied p_z states (p_z^{u+}) and p_y^{o+}, between spin-up unoccupied p_y states (p_y^{u+}) and p_x^{o+}, as well as between spin-up unoccupied p_x states (p_x^{u+}) and p_y^{o+}. Supplementary Table 3 also indicates that the matrix element difference between p_z^{u+} and p_y^{o+} is −1, implying a negative contribution to MAE from the p_y and p_z hybridization. On the other hand, the matrix element difference between $p_{y(x)}^{u+}$ and $p_{x(y)}^{o+}$ equals 1, resulting in a positive contribution to MAE from the p_x and p_y hybridization. Considering that the energy difference between p_z^{u+} and p_y^{o+} (Δ_{yz}) is smaller than that between $p_{y(x)}^{u+}$ and $p_{x(y)}^{o+}$ (Δ_{xy}), as shown in Supplementary Fig. 11a, according to Eq. (2), the negative contribution to MAE outweighs the positive one, which is consistent with the orbital-resolved MAE of the Bi_1 atom. Since the Te_2 and Te_3 atoms have similar DOS distributions, as illustrated in Supplementary Fig. 11b, c, we chose the Te_2 atom as the representative for our investigation. The main unoccupied and occupied states near the Fermi level are determined by spin-up and spin-down states, respectively. Notably, the spin-up unoccupied state is mainly dominated by the $p_{x(y)}^{u+}$, and thus its hybridizations between spin-down occupied p_z and $p_{x,y}$ states (p_z^{o-} and $p_{y(x)}^{o-}$) can contribute to the MAE. As listed in Supplementary Table 3, matrix element differences between p_y^{u+} and p_z^{o-}, as well as between $p_{x(y)}^{u+}$ and $p_{y(x)}^{o-}$, are equal to 1 and −1, respectively. The energy differences between p_y^{u+} and p_z^{o-}, as well as between $p_{x(y)}^{u+}$ and $p_{y(x)}^{o-}$ are similar. However, as indicated by the DOS, the strength of $p_{y(x)}^{o-}$ is greater than that of p_z^{o-}, and thus the hybridization between $p_{x(y)}^{u+}$ and $p_{y(x)}^{o-}$ plays a major role. As a result, both Te_2 and Te_3 atoms contribute to the IMA, as illustrated in Supplementary Fig. 10b, c.

When the In_2Se_3 monolayer is flipped to the P↓ state, considerable charge transfer from VBi_2Te_4 to In_2Se_3 (details below) can induce a shift of p orbital occupied states towards the Fermi level for Bi_1, Te_2, and Te_3 atoms. This results in a redistribution of the DOS, see Supplementary Fig. 11, which has the potential to alter the MAE of these atoms. For the Bi_1 atom, the SOC-induced total energy variations are primarily governed by the hybridization between spin-down occupied and unoccupied states. According to Supplementary Table 3, the matrix element difference between spin-down unoccupied $p_{x,y}$ state ($p_{x(y)}^{u-}$) and $p_{y(x)}^{o-}$ remains equal to 1, suggesting a positive contribution to MAE from the hybridization between p_x and p_y orbitals. Notably, Supplementary Fig. 10d reveals a disappearance of the hybridization between p_y and p_z orbitals, which is replaced by a positive contribution from the p_x and p_z hybridization, contradicting the data presented in Supplementary Table 3. The explanation of this phenomenon may necessitate the incorporation of higher-order terms in Eq. (2). Since the hybridization between p_x and p_z orbitals does not affect our conclusions, we will not discuss it here. In this context, the Bi_1 atom exhibits a positive MAE contribution, thereby contributing to the PMA. For the Te_2 atom, the spin-up electronic states intersect with the Fermi level, and the p^{u+} state closest to the Fermi level play a significant role in contributing to the MAE when interacting with the p^{o+} state. As listed in Supplementary Table 3, matrix element differences between p_y^{u+} and p_z^{o+}, as well as between $p_{x(y)}^{u+}$ and $p_{y(x)}^{o+}$, can be obtained, featuring −1 and 1, respectively. However, the energy difference between $p_{x(y)}^{u+}$ and $p_{y(x)}^{o+}$ is smaller than that between p_y^{u+} and p_z^{o+}, resulting in a stronger contribution of PMA over IMA, as shown in Supplementary Fig. 10e. The Te_3 atom demonstrates similar results to the Te_2 atom, see Supplementary Figs. 10f and 11c. Consequently, the transition of magnetic anisotropy in the VBi_2Te_4 monolayer caused by the polarization reversal of the In_2Se_3 monolayer can be attributed to the changes in hybridizations between p orbitals of Bi_1, Te_2, and Te_3 atoms.

Furthermore, the alteration of electronic properties in the heterostructure induced by polarization switching is further explained by considering the band alignment between two monolayers and the interfacial charge transfer. As shown in Supplementary Fig. 12a, b, the VBi_2Te_4 monolayer is symmetric with an identical electrostatic potential on both sides. In contrast, the In_2Se_3 monolayer displays an asymmetric structure with noticeable differences in electrostatic potential along the out-of-plane direction, resulting in a 1.2 eV discrepancy in work function between its two sides. Through integrating 2D VBi_2Te_4 and In_2Se_3 into the vdW heterostructure, the spatial inversion symmetry is broken because of the presence of ferroelectricity. Therefore, different band alignments are generated for the two opposite polarized states. For the P↑ configuration, as depicted in Fig. 5a, the valence band of the VBi_2Te_4 monolayer in both spin-up and spin-down channels are energetically lower than the conduction band of the In_2Se_3 monolayer, which hinders charge transfer between VBi_2Te_4 and In_2Se_3. Despite this fact, a weak charge transfer and redistribution occur at the interface due to the small electrostatic potential difference (ΔV) and associated built-in electric field at the interface, see Fig. 5c and Supplementary Fig. 12c. However, this subtle effect is insufficient to induce any qualitative changes in the electronic properties; hence, both VBi_2Te_4 and In_2Se_3 monolayers tend to retain their intrinsic semiconducting nature. By switching the In_2Se_3 monolayer to the P↓ state, the conduction band edge of the In_2Se_3 becomes lower than the spin-up valence band of the VBi_2Te_4, while still remaining higher than its spin-down valence band, see Fig. 5b. Accompanied by a significant increase in interfacial ΔV, a large amount of charge transfer takes place at the interface, as depicted in Fig. 5d and Supplementary Fig. 12d. This charge transfer is chiefly characterized by the injection of electrons from the spin-up channel of the VBi_2Te_4 monolayer into the In_2Se_3 monolayer, which results in partial filling of the spin-up subband and yields fully spin-polarized hole pockets for the VBi_2Te_4 monolayer. In this context, the VBi_2Te_4 monolayer exhibits metallic and semiconducting characters in spin-up and spin-down channels, respectively, giving rise to a half-metallic characteristic. The 2D In_2Se_3 behaves as a metal due to the electron injection. Therefore, the phase transition from a semiconductor to a half-metal for the VBi_2Te_4 monolayer within the heterostructure arises synergistically from the polarization switching-induced alteration of band alignment and the charge transfer occurring at the interface. In brief, even within the framework of weak vdW interlayer interaction, the VBi_2Te_4/In_2Se_3 heterostructure can still achieve the seemingly counter-intuitive phenomenon of strong magnetoelectric coupling.

Recently, ferroelectric memory has garnered significant attention as a highly promising member within the realm of memory technologies. Compared to other types of storage devices, such as magnetic memory, ferroelectric memory exhibits superiority in the data writing process achieved by changing the polarized state of ferroelectrics. Nevertheless, the data reading process in

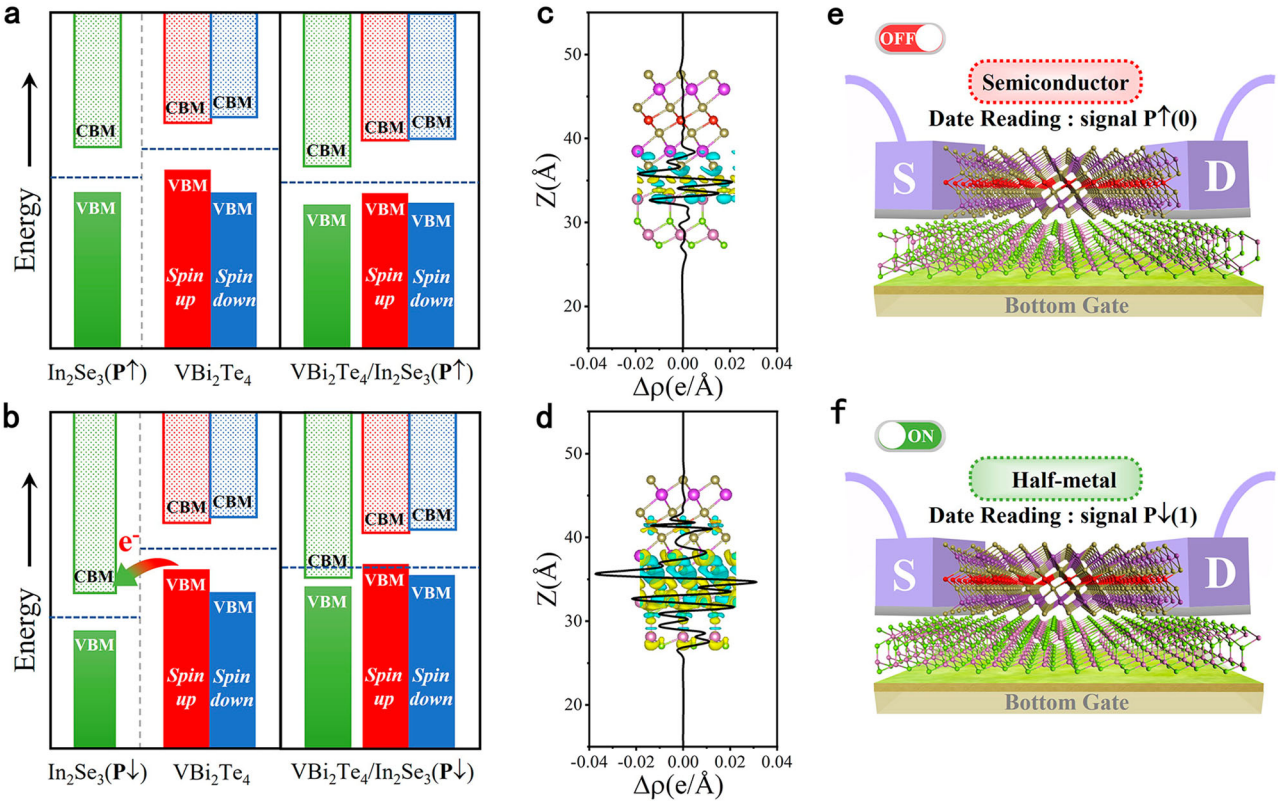

Fig. 5 Origin of phase transition and device prototype. a, **b** Band alignment of the VBi_2Te_4/In_2Se_3 heterostructure with P↑ and P↓ states. **c**, **d** Plane-averaged charge density difference and differential charge density distributions of the VBi_2Te_4/In_2Se_3 heterostructure with P↑ and P↓ states. The isosurface value is 0.0003 eÅ^{-3}. **e**, **f** Schematic representation of multiferroic memory device designed based on the VBi_2Te_4/In_2Se_3 heterostructure. The data writing process relies on the ferroelectric In_2Se_3, while the data reading process is realized by detecting the electric or optical signal of the VBi_2Te_4 monolayer.

ferroelectric memory is destructive, which poses great challenges to the flexibility and service life of storage devices. To address this drawback, a prototype of a memory device based on the VBi_2Te_4/In_2Se_3 multiferroic vdW heterostructure for high-density data storage is proposed, as depicted in Fig. 5e, f. In this conceptual device, data writing is achieved by flipping the electric polarization of the ferroelectric In_2Se_3, which retains the advantage of ferroelectric memory in data writing. The ferroelectric control of electronic properties in the VBi_2Te_4 monolayer provides a remarkable avenue for realizing data reading. When the electric polarization of the In_2Se_3 monolayer is upward, the VBi_2Te_4 monolayer behaves as a semiconductor and no electric signal is detected. We denote this state as the 'OFF' or '0' state of the device. In contrast, when the 2D In_2Se_3 is driven into the P↓ state, the VBi_2Te_4 monolayer becomes conductive due to its half-metallicity, allowing spin-polarized holes to propagate through the channel layer. This corresponds to the 'ON' or '1' state. Thus, in this multiferroic memory, the data reading process is achieved by converting the polarized states of the In_2Se_3 monolayer into the conducting state of the VBi_2Te_4 monolayer and checking it, which effectively avoids the destructive effect caused by detecting ferroelectric polarization. Additionally, since 2D XY and Heisenberg ferromagnets exhibits distinct optical signals, data reading in the device can also be achieved by checking the magnetoelectric coupling-induced signal differences in the VBi_2Te_4 monolayer. As a matter of fact, the proposed device prototype is also applicable for designing high-performance field effect transistor (FET). The ability to readily control the conducting state in the VBi_2Te_4/In_2Se_3 heterostructure is likely to result in a high on-off ratio for the FET, and more importantly, the whole regulation process is nonvolatile. The interfacial magnetoelectric coupling also endows the VBi_2Te_4/In_2Se_3 heterostructure with great potential for exploring modern magnetic and resistive memories.

Effects of strain and interlayer distance variations

In experimental synthesis or device fabrication, the magnetoelectric coupling of the VBi_2Te_4/In_2Se_3 heterostructure may be affected by several factors, such as a small amount of artificial strain. Therefore, investigating the effect of biaxial strain on the magnetic and electronic properties of the heterostructure is of particular interest. Figure 6a displays the variation of E_{MAE} as a function of biaxal strain. For the heterostructure with up-polarized In_2Se_3, the E_{MAE} slightly increases under compressive strain, but exhibits a decreasing trend under tensile strain. The sign of E_{MAE} remains unchanged, suggesting that the characteristic of 2D XY ferromagnet is sustained for the VBi_2Te_4 monolayer. By comparison, in the P↓ configuration, biaxial strain can effectively modulate the E_{MAE}. With increasing compressive strain, the E_{MAE} is continuously enhanced, indicating further stabilization of long-range FM ordering in the VBi_2Te_4 monolayer. However, when tensile strain is adopted, the E_{MAE} first undergoes a sign change and then increases obviously as tensile strain increases, implying that the VBi_2Te_4 monolayer reverts to a 2D XY ferromagnet. Hence, in the stretched VBi_2Te_4/In_2Se_3 heterostructure, the magnetoelectric coupling effect is eliminated since the IMA of the VBi_2Te_4 becomes immune to polarization switching. To elucidate the sign change of MAE in the P↓ configuration, we plot the atom-resolved MAE of the VBi_2Te_4 monolayer subjected to different strains in Fig. 6b. One can see that the tensile strain-induced IMA is attributed to the sign reversal of the MAE contributions from Te_1, Te_2, and Te_3 atoms. Besides, both compressive and tensile strains can enhance

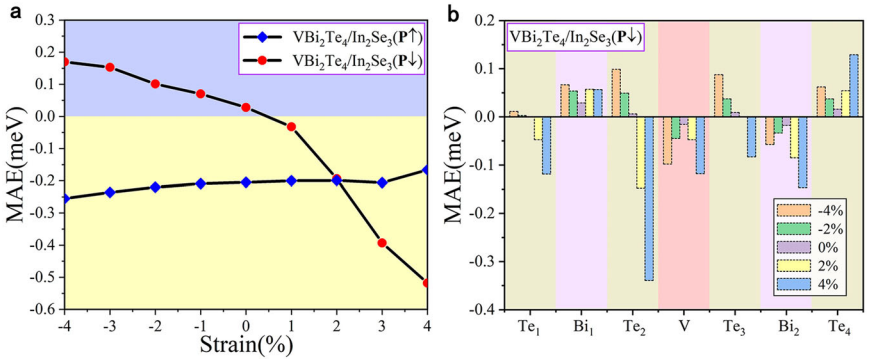

Fig. 6 Strain-induced change in MAE. a Calculated MAE of the VBi_2Te_4/In_2Se_3 heterostructure with P↑ and P↓ states in term of the biaxial strain. **b** Atom-resolved MAE of the VBi_2Te_4 monolayer in the heterostructure subjected to various strains.

the MAE contribution of all atoms, providing a reasonable explanation for the observed increase in MAE under strains. Supplementary Figs. 13 and 14 present the band structures of P↑ and P↓ configurations under different strains. The results reveal that the semiconductor property of the P↑ configuration is preserved intact with strain ranging from −4% to 4%. The band gap exhibits an increasing trend under compressive strain and a decreasing trend under tensile strain. In the P↓ configuration, the VBi_2Te_4 monolayer retains its half-metallicity under compressive strain, and more importantly, the hole doping concentration is enhanced accordingly. This phenomenon is mainly ascribed to the increased charge transfer from VBi_2Te_4 to In_2Se_3 monolayers. The employment of compressive strain would shorten the bond length, resulting in more extend energy band dispersions for VBi_2Te_4 and In_2Se_3. Under this circumstance, the difference between the spin-up valence band edge of the VBi_2Te_4 and the conduction band edge of the In_2Se_3 is enhanced, thereby promoting charge transfer at the interface. In contrast, tensile strain renders a more localized energy band dispersion, which leads to a reduction in interfacial charge transfer. Thus, the hole doping weakens with increasing tensile strain, and the VBi_2Te_4 monolayer transforms into a semiconductor at a critical strain of 4%. In light of the above findings, the VBi_2Te_4/In_2Se_3 heterostructure exhibits favorable characteristics in both equilibrium and compression states, rendering it highly suitable for practical applications.

To gain insight into the origin of changes in MAE induced by tensile strain for Te_1, Te_2, and Te_3 atoms, we conduct a comparative analysis of orbital-resolved MAE for the P↓ configuration under 0% and 4% tensile strains. As shown in Supplementary Fig. 15, for the Te_1 atom in the pristine heterostructure, the contribution of hybridization between p orbitals to MAE is almost negligible. However, when subjected to tensile strain, there is a significantly enhancement of the hybridizations between p_y and p_z orbitals, as well as between p_x and p_y orbitals. Notice that the former and latter constitute IMA and PMA, respectively, with the former being strong than the latter, thereby resulting in the contribution of the Te_1 atom to the IMA. While the sign change of MAE for the Te_2 atom under tensile strain can be attributed to a remarkable increase in the hybridization between p_y and p_z orbitals, accompanied by the sign reversal of the hybridization between p_x and p_y orbitals. This latter effect is also responsible for the observed MAE change of the Te_3 atom. We further provide a qualitative explanation for the MAE changes of Te_1, Te_2, and Te_3 atoms using second-order perturbation theory. The projected DOS of these Te atoms in the P↓ configuration under a 4% tensile strain is shown in Supplementary Fig. 16. Starting from the Te_1 atom, it can be seen that both occupied and unoccupied states near the Fermi level are determined by the spin-up state. This suggests that the hybridization between p^{o+} and p^{u+} dominates the SOC-induced total energy changes. Therefore, the Te_1 atom exhibits a mechanism similar to that of the Bi_1 atom in pristine P↑ configuration. For the Te_2 atom, tensile strain drives its spin-up occupied p_z orbital to move towards the Fermi level, decreasing the energy difference between p_y^{u+} and p_z^{o+}. This leads to an increase in the hybridization between p_y and p_z orbitals, which contributes to the IMA. In addition, the enhancement of the spin-down occupied state $p_{x(y)}^{o-}$ in both Te_2 and Te_3 atoms can be observed under tensile strain, which facilitates its interaction with $p_{x(y)}^{u+}$. As listed in Supplementary Table 3, the matrix element difference between $p_{x(y)}^{o-}$ and $p_{y(x)}^{u+}$ is −1, indicating the p_x and p_y hybridization provides a negative MAE contribution, which aligns with the orbital-resolved MAE of Te_2 and Te_3 atoms.

The preceding discussion has confirmed the sign change of MAE for the VBi_2Te_4 monolayer upon reversing the polarization of the In_2Se_3 monolayer from upward to downward. This change is attributed to modifications in interlayer coupling induced by interface alternation. Given the strong correlation between interlayer distance and interlayer coupling strength, it is essential to study the influence of variations in interlayer distance (Δd) on the magnetic anisotropy of the VBi_2Te_4 monolayer. Prior to that, we first investigate the relationship between amount of electron transfer (Δe) from VBi_2Te_4 to In_2Se_3 monolayers and Δd. As shown in Supplementary Fig. 17a, the increase (decrease) in Δe is observed as Δd decreases (increases), regardless of P↑ and P↓ configurations. This phenomenon demonstrates that the reduction (expansion) of interlayer distance enhances (weakens) the interlayer coupling, thereby facilitating (impeding) interfacial electron transfer. Supplementary Fig. 17b presents the variation of E_{MAE} as a function of Δd. For the P↑ configuration, there is a gradual increase in E_{MAE} observed with decreasing interlayer distance. Conversely, when the interlayer distance is increased, the E_{MAE} decreases gradually with a slight fluctuation. Throughout this process, the consistently negative sign of E_{MAE} indicates that the IMA of the VBi_2Te_4 monolayer is immune to Δd. On the other hand, in the P↓ configuration, an increased interlayer distance leads to a continuous reduction in E_{MAE}, while a decreased interlayer distance initially increases and then diminishes the E_{MAE}. When the interlayer distance is reduced by 0.3 Å, the E_{MAE} can reach up to 0.04 meV per unit cell. Nevertheless, a transition from PMA to IMA can be observed in the VBi_2Te_4 monolayer when the interlayer distance decreases by more than 0.6 Å, as evidenced by the sign change of E_{MAE}. More importantly, the half-metallicity of the VBi_2Te_4 monolayer within the P↓ configuration remains unaffected by variations in interlayer distance, as shown in Supplementary Fig. 18. In a word, manipulating the interlayer distance offers a viable strategy to modulate the MAE of the heterostructure.

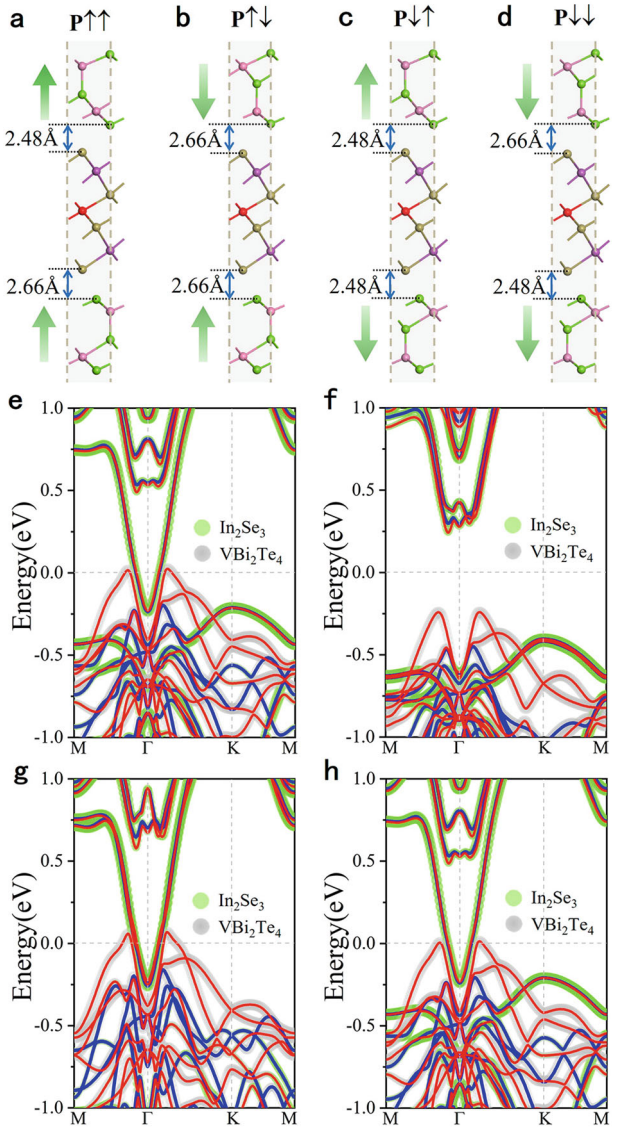

Fig. 7 Basic properties of the $In_2Se_3/VBi_2Te_4/In_2Se_3$. **a**–**d** Geometric structures of the $In_2Se_3/VBi_2Te_4/In_2Se_3$ heterostructure in P↑↑, P↑↓, P↓↑, and P↓↓ configurations. **e**–**h** Calculated band structures of the $In_2Se_3/VBi_2Te_4/In_2Se_3$ heterostructure in P↑↑, P↑↓, P↓↑, and P↓↓ configurations. The red and blue lines represent spin-up and spin-down states, respectively.

$In_2Se_3/VBi_2Te_4/In_2Se_3$ and VBi_2Te_4/bi-In_2Se_3 heterostructures

Considering that the VBi_2Te_4 monolayer has two surfaces, another form of multiferroic vdW heterostructure is proposed by sandwiching it between two ferroelectric In_2Se_3 monolayers. This heterostructure, denoted as $In_2Se_3/VBi_2Te_4/In_2Se_3$, is anticipated to provide more opportunities for nonvolatile electrical control over the magnetic and electronic properties of 2D VBi_2Te_4. Four polarization configurations, namely, P↑↑, P↑↓, P↓↑ and P↓↓, are designed for the $In_2Se_3/VBi_2Te_4/In_2Se_3$ heterostructure based on the energetically stable stacking pattern between VBi_2Te_4 and In_2Se_3 monolayers. The geometric structures and optimized interlayer distances of different configurations are illustrated in Fig. 7a–d. Interestingly, we find a strong correlation between the interface type and the interlayer distance in the heterostructure. For instance, the upper and lower interfaces of the P↑↑ configuration correspond to the interfaces of the VBi_2Te_4/In_2Se_3 heterostructure with P↓ and P ↑ states, respectively, while the interlayer distance exhibits the same phenomenon. This fundamental law is also applicable to the P↑↓, P↓↑ and P↓↓ configurations. We then calculate the E_b of the $In_2Se_3/VBi_2Te_4/In_2Se_3$ heterostructure by $E_b = (E_{In_2Se_3/VBi_2Te_4/In_2Se_3} - E_{VBi_2Te_4} - 2E_{In_2Se_3})/S$ and estimate that it is approximately -0.27 eV Å^{-2}, which is smaller than that of the VBi_2Te_4/In_2Se_3 heterostructure. In the following, we investigate the magnetic and electronic properties of the $In_2Se_3/VBi_2Te_4/In_2Se_3$ heterostructure. For the P↑↑ configuration, the value of E_{MAE} is calculated to be 0.02 meV per unit cell, revealing that the VBi_2Te_4 monolayer in the heterostructure belongs to a 2D Heisenberg ferromagnet. The band structure in Fig. 7e shows that the VBi_2Te_4 monolayer exhibits a hole doping-induced half-metallic character. The hole doping is primarily attributed to the transfer of massive electrons from the VBi_2Te_4 monolayer to the top In_2Se_3 monolayer, see Supplementary Fig. 19a. In contrast, the electron transfer at the lower interface is very limited. As a result, in the $In_2Se_3/VBi_2Te_4/In_2Se_3$ with the P↑↑ state, the upper interface plays a dominant role in determining the magnetic and electronic properties of the VBi_2Te_4 monolayer, thereby leading to the PMA in the VBi_2Te_4 monolayer. Then we turn to the P↑↓ configuration whose upper and lower interfaces coincide with that of the VBi_2Te_4/In_2Se_3 heterostructure in the P↑ configuration. The E_{MAE} is calculated to be −0.20 meV per unit cell, demonstrating the IMA in the VBi_2Te_4 monolayer. A semiconducting property with an indirect band gap of 0.48 eV is obtained for the heterostructure, as presented in Fig. 7f. As expected, there is only a small amount of charge transfer at interfaces, see Supplementary Fig. 19b. In the P↓↑ configuration, both the upper and lower interfaces are identical to that of the VBi_2Te_4/In_2Se_3 heterostructure with the P↓ state. It turns out that the value of E_{MAE} is 0.18 meV per unit cell, which is improved by an order of magnitude compared to the VBi_2Te_4/In_2Se_3 heterostructure. In this scenario, the VBi_2Te_4 monolayer transforms into a 2D Heisenberg ferromagnet with a more stable long-range FM ordering. From the band structure given in Fig. 7g, one can see that the VBi_2Te_4 monolayer possesses half-metallic behavior, and more interestingly, there is a pronounced increase in hole doping concentration. This is because abundant electrons are simultaneously transferred from the VBi_2Te_4 monolayer to both the top and bottom In_2Se_3 monolayers, as shown in Supplementary Fig. 19c. When the $In_2Se_3/VBi_2Te_4/In_2Se_3$ heterostructure is in the P↓↓ configuration, it exhibits the same magnetic and electronic properties as those of the P↑↑ configuration because of the existence of spatial inversion symmetry, as illustrated in Fig. 7h and Supplementary Fig. 19d. Furthermore, the electronic properties of these four polarization configurations remain largely unchanged by the inclusion of SOC effect, with only a slight decrease in band gap for the P↑↓ configuration, see Supplementary Fig. 20. To gain a better understanding of the electronic properties, we plot the band alignments between VBi_2Te_4 and In_2Se_3 in Supplementary Fig. 21. To be brief, in the $In_2Se_3/VBi_2Te_4/In_2Se_3$ heterostructure, the magnetic and electronic properties are predominantly governed by a synergistic interplay between the upper and lower interfaces.

Additionally, we explore the influence of varying the thickness of ferroelectric In_2Se_3 on the physical properties of the VBi_2Te_4 monolayer. To achieve this, we propose a VBi_2Te_4/bi-In_2Se_3 heterostructure by introducing an additional In_2Se_3 monolayer at the bottom of the VBi_2Te_4/In_2Se_3. Two opposite polarized states are considered and denoted as bi-P↑↑ and bi-P↓↓, as shown in Fig. S22a, b. The calculated E_b of the VBi_2Te_4/bi-In_2Se_3 heterostructure is approximately -0.26 eV Å^{-2}. The MAE calculation results indicate that the VBi_2Te_4 monolayer exhibits IMA and PMA in bi-P↑↑ and bi-P↓↓ configurations, respectively, accompanied by corresponding E_{MAE} of −0.12 and 0.12 meV per unit cell. This discovery aligns with the observed behavior in the VBi_2Te_4/In_2Se_3 heterostructure, revealing that even with an increased number of ferroelectric layers, the easy magnetization axis of the VBi_2Te_4 monolayer remains robust. The band structures of the VBi_2Te_4/bi-

In_2Se_3 heterostructure with different polarized states are illustrated in Supplementary Fig. 22 c, d. It can be observed that the bi-P↑↑ configuration exhibits metallic behavior, contributed by the In_2Se_3 bilayer, as shown in Supplementary Fig. 22c. When the electric polarization of the In_2Se_3 bilayer is oriented downward, the VBi_2Te_4/bi-In_2Se_3 shows similar electronic properties to those of the VBi_2Te_4/In_2Se_3 heterostructure with the P↓ state, where the VBi_2Te_4 monolayer and In_2Se_3 bilayer possess half-metallicity and metallicity, respectively, see Supplementary Fig. 22d. However, compared to the VBi_2Te_4/In_2Se_3 heterostructure, the half-metallicity of the VBi_2Te_4 monolayer within the VBi_2Te_4/bi-In_2Se_3 heterostructure is enhance, characterized by a higher hole doping concentration. This enhancement is attributed to a greater electron transfer from the VBi_2Te_4 monolayer to the In_2Se_3 bilayer, which is facilitated by an increased number of ferroelectric layers, as shown in Supplementary Fig. 22e, f. Thus, the VBi_2Te_4/bi-In_2Se_3 heterostructure can also achieve synchronous control of both magnetic anisotropy and half-metallicity in the VBi_2Te_4 monolayer, enabling desirable magnetoelectric coupling.

It is noteworthy that the In_2Se_3 monolayer (bilayer) exhibits a ferroelectric metal phase in both VBi_2Te_4/In_2Se_3, In_2Se_3/VBi_2Te_4/In_2Se_3, and VBi_2Te_4/bi-In_2Se_3 heterostructures. The screening effect typically eliminates the possibility of ferroelectric polarization switching in metallic bulk materials; however, this effect becomes negligible in atomically thin films due to the profound penetration of the external electric field. Experimental evidence has successfully demonstrated the switchable behavior in a 2D ferroelectric metal[21]. Therefore, the polarization reversal in the In_2Se_3 monolayer (bilayer) within heterostructures can be achieved by applying an external electric field, irrespective of its metallicity.

In summary, we have designed multiferroic vdW heterostructures consisting of FM VBi_2Te_4 and ferroelectric In_2Se_3 monolayers, and examined the corresponding magnetoelectric coupling by first-principles calculations. By reversing the electric polarization of the In_2Se_3 monolayer, the magnetic anisotropy of the VBi_2Te_4 monolayer can be switched between easy-plane and easy-axis states, enabling transformation of the VBi_2Te_4 from 2D XY to Heisenberg ferromagnets. More interestingly, with the reversal of easy magnetization axis, the VBi_2Te_4 monolayer also undergoes a transition from a semiconductor to a half-metal. This fascinating phenomenon is essentially attributed to the band alignment and charge transfer between VBi_2Te_4 and In_2Se_3 monolayers. A conceptual memory device is proposed for nonvolatile data storage based on the multiferroic vdW heterostructure. Additionally, biaxial strain has been demonstrated as an effective avenue to tune the half-metallicity and MAE of the VBi_2Te_4 monolayer in the heterostructure. The present work provides potential candidates for achieving nonvolatile electrical control of magnetic anisotropy and half-metallicity, which paves the way for the exploitation of high-performance nanodevices.

METHODS

Geometry optimization and electronic structure calculations

All first-principles calculations were performed using the Vienna ab initio simulation package (VASP) within the framework of density functional theory (DFT)[45,46]. The electron-ion interaction was described by the projector-augmented wave (PAW) pseudopotentials method[47,48], and the generalized gradient approximation (GGA) of Perdew-Burke-Ernzerhof (PBE) parametrization was implemented for the exchange correlation functional[49]. The cutoff energy of the plane-wave basis was set to 400 eV. The first Brillouin zone was sampled by employing a centered 25×25×1 Monkhorst-Pack *k*-point mesh. To avoid interaction between neighboring periodic images, a vacuum region up to 70 Å was adopted along the *z* direction. The atomic positions were fully relaxed until the force on each atom was less than 0.001 eV A^{-1}, and the convergence criteria for energy was set as 1×10^{-5} eV. The GGA + *U* scheme was utilized to treat the strong exchange correlations of the magnetic atom[50], and the U_{eff} is selected to be 3.0 eV for the V-*d* orbital, according to previous investigations[31,33]. The DFT-D3 method of Grimme was adopted to describe the interlayer vdW interactions[51,52]. To access the reliability of DFT-D3 in comparison with other methods, we also employed DFT-D2 and optPBE-vdW methods to examine the systems investigated in this study[53,54]. Despite slight variations in interlayer distance under different methods, the calculated magnetic anisotropy and band structure of heterostructure remains nearly identical to those obtained using DFT-D3 method, as shown in Supplementary Table 4 and Fig. 23, thereby validating the reliability of DFT-D3 method. Dipole correction was incorporated in the calculation of the work function, whereas it was omitted from the calculation of heterostructures. This is because even with dipole correction considered, the physical properties of the heterostructure and our main conclusion will not be affected, as illustrated in Supplementary Fig. 24.

Polarization, NEB, and phonon spectrum calculations

The out-of-plane polarization was calculated by directly integrating the charge density over the whole structure in consideration of the presence of a vacuum region. It can be defined as:

$$P = \frac{1}{S}\int z\rho(z)dz \tag{3}$$

where ρ is the charge density, S represents the plane area of the 2D supercell, and z is the coordinate. The ferroelectric transition path and energy barrier were calculated utilizing the climbing-image nudged elastic band (NEB) method[55,56]. Phonon dispersions were calculated using the finite displacement method as implemented in the PHONOPY code[57], in which a $3\times3\times1$ supercell was employed.

DATA AVAILABILITY

The authors declare that the main data supporting the findings of this study are available within the article and its Supplementary Information files.

CODE AVAILABILITY

The central codes used in this paper are VASP. Detailed information related to the license and user guide are available at https://www.vasp.at.

Received: 19 June 2023; Accepted: 28 November 2023;
Published online: 15 December 2023

REFERENCES

1. Huang, B. et al. Layer-dependent ferromagnetism in a van der Waals crystal down to the monolayer limit. *Nature* **546**, 270–273 (2017).
2. Gong, C. et al. Discovery of intrinsic ferromagnetism in two-dimensional van der Waals crystals. *Nature* **546**, 265–269 (2017).
3. Deng, Y. et al. Gate-tunable room-temperature ferromagnetism in two-dimensional Fe_3GeTe_2. *Nature* **563**, 94–99 (2018).
4. O'Hara, D. J. et al. Room Temperature Intrinsic Ferromagnetism in Epitaxial Manganese Selenide Films in the Monolayer Limit. *Nano Lett.* **18**, 3125–3131 (2018).
5. Jiang, S., Shan, J. & Mak, K. F. Electric-field switching of two-dimensional van der Waals magnets. *Nat. Mater.* **17**, 406–410 (2018).
6. Huang, B. et al. Electrical control of 2D magnetism in bilayer CrI_3. *Nat. Nanotechnol.* **13**, 544–548 (2018).
7. Jiang, S., Li, L., Wang, Z., Mak, K. F. & Shan, J. Controlling magnetism in 2D CrI_3 by electrostatic doping. *Nat. Nanotechnol.* **13**, 549–553 (2018).
8. Verzhbitskiy, I. A. et al. Controlling the magnetic anisotropy in $Cr_2Ge_2Te_6$ by electrostatic gating. *Nat. Electron.* **3**, 460–465 (2020).

9. Du, L. et al. 2D proximate quantum spin liquid state in atomic-thin α-$RuCl_3$. *2D Mater.* **6**, 015014 (2019).
10. Wang, J. et al. Physical Vapor Transport Growth of Antiferromagnetic $CrCl_3$ Flakes Down to Monolayer Thickness. *Adv. Sci.* **10**, 2203548 (2023).
11. Kim, H. H. et al. Evolution of interlayer and intralayer magnetism in three atomically thin chromium trihalides. *Proc. Natl Acad. Sci. USA* **116**, 11131–11136 (2019).
12. Bedoya-Pinto, A. et al. Intrinsic 2D-XY ferromagnetism in a van der Waals monolayer. *Science* **374**, 616–620 (2021).
13. Mashhadi, S. et al. Electrical Transport Signature of the Magnetic Fluctuation-Structure Relation in α-$RuCl_3$ Nanoflakes. *Nano Lett.* **18**, 3203–3208 (2018).
14. Mermin, N. D. & Wagner, H. Absence of Ferromagnetism or Antiferromagnetism in One- or Two-Dimensional Isotropic Heisenberg Models. *Phys. Rev. Lett.* **17**, 1133–1136 (1966).
15. Guo, S.-D., Guo, X.-S., Wang, G.-Z., Cheng, K. & Ang, Y.-S. Electric-field induced magnetic-anisotropy transformation to achieve spontaneous valley polarization. *J. Mater. Chem. C.* **10**, 16363–16369 (2022).
16. Webster, L. & Yan, J.-A. Strain-tunable magnetic anisotropy in monolayer $CrCl_3$, $CrBr_3$, and CrI_3. *Phys. Rev. B* **98**, 144411 (2018).
17. Xue, F., Hou, Y., Wang, Z. & Wu, R. Two-dimensional ferromagnetic van der Waals $CrCl_3$ monolayer with enhanced anisotropy and Curie temperature. *Phys. Rev. B* **100**, 224429 (2019).
18. Cui, Q., Zhu, Y., Liang, J., Cui, P. & Yang, H. Spin-valley coupling in a two-dimensional VSi_2N_4 monolayer. *Phys. Rev. B* **103**, 085421 (2021).
19. Tian, Y. et al. Lanthanide atoms doped arsenene monolayer: Enhanced magnetic anisotropies, huge magnetic moments and significant strain-modulated effects. *J. Rare Earths* https://doi.org/10.1016/j.jre.2023.10.024 (2023).
20. Chandrasekaran, A., Mishra, A. & Singh, A. K. Ferroelectricity, Antiferroelectricity, and Ultrathin 2D Electron/Hole Gas in Multifunctional Monolayer MXene. *Nano Lett.* **17**, 3290–3296 (2017).
21. Fei, Z. et al. Ferroelectric switching of a two-dimensional metal. *Nature* **560**, 336–339 (2018).
22. Liu, F. et al. Room-temperature ferroelectricity in $CuInP_2S_6$ ultrathin flakes. *Nat. Commun.* **7**, 12357 (2016).
23. Wan, S. et al. Nonvolatile Ferroelectric Memory Effect in Ultrathin α-In_2Se_3. *Adv. Funct. Mater.* **29**, 1808606 (2019).
24. Yuan, S. et al. Room-temperature ferroelectricity in $MoTe_2$ down to the atomic monolayer limit. *Nat. Commun.* **10**, 1775 (2019).
25. Zhou, Y. et al. Out-of-Plane Piezoelectricity and Ferroelectricity in Layered α-In_2Se_3 Nanoflakes. *Nano Lett.* **17**, 5508–5513 (2017).
26. Zhao, Y., Zhang, J. J., Yuan, S. & Chen, Z. Nonvolatile Electrical Control and Heterointerface-Induced Half-Metallicity of 2D Ferromagnets. *Adv. Funct. Mater.* **29**, 1901420 (2019).
27. Yang, B. et al. Realization of semiconducting layered multiferroic heterojunctions via asymmetrical magnetoelectric coupling. *Phys. Rev. B* **103**, L201405 (2021).
28. Sun, W., Wang, W., Chen, D., Cheng, Z. & Wang, Y. Valence mediated tunable magnetism and electronic properties by ferroelectric polarization switching in 2D FeI_2/In_2Se_3 van der Waals heterostructures. *Nanoscale* **11**, 9931–9936 (2019).
29. Wang, Y. et al. Switchable half-metallicity in A-type antiferromagnetic NiI_2 bilayer coupled with ferroelectric In2Se3. *npj Comput. Mater.* **8**, 218 (2022).
30. Jiang, P. et al. Ferroelectric control of electron half-metallicity in A-type antiferromagnets and its application to nonvolatile memory devices. *Phys. Rev. B* **102**, 245417 (2020).
31. Li, J. et al. Intrinsic magnetic topological insulators in van der Waals layered $MnBi_2Te_4$-family materials. *Sci. Adv.* **5**, eaaw5685 (2019).
32. Li, Y., Jiang, Z., Li, J., Xu, S. & Duan, W. Magnetic anisotropy of the two-dimensional ferromagnetic insulator $MnBi_2Te_4$. *Phys. Rev. B* **100**, 134438 (2019).
33. Zhu, W. et al. Quantum anomalous Hall insulator state in ferromagnetically ordered $MnBi_2Te_4$/VBi_2Te_4 heterostructures. *Phys. Rev. B* **102**, 085111 (2020).
34. Ding, W. et al. Prediction of intrinsic two-dimensional ferroelectrics in In_2Se_3 and other III_2-VI_3 van der Waals materials. *Nat. Commun.* **8**, 14956 (2017).
35. Liu, J. & Pantelides, S. T. Pyroelectric response and temperature-induced α-β phase transitions in α-In_2Se_3 and other α-III_2VI_3 (III = Al, Ga, In; VI = S, Se) monolayers. *2D Mater.* **6**, 025001 (2019).
36. Zhang, Z. et al. Direct Photoluminescence Probing of Ferromagnetism in Monolayer Two-Dimensional $CrBr_3$. *Nano Lett.* **19**, 3138–3142 (2019).
37. Li, Z. & Zhou, B. Theoretical investigation of nonvolatile electrical control behavior by ferroelectric polarization switching in two-dimensional $MnCl_3$/$CuInP_2S_6$ van der Waals heterostructures. *J. Mater. Chem. C.* **8**, 4534–4541 (2020).
38. Liu, W.-R. et al. Magnetic anisotropy and ferroelectric-driven magnetic phase transition in monolayer $Cr_2Ge_2Te_6$. *Nanoscale* **14**, 3632–3643 (2022).
39. Gong, C., Kim, E. M., Wang, Y., Lee, G. & Zhang, X. Multiferroicity in atomic van der Waals heterostructures. *Nat. Commun.* **10**, 2657 (2019).
40. Xue, F., Wang, Z., Hou, Y., Gu, L. & Wu, R. Control of magnetic properties of $MnBi_2Te_4$ using a van der Waals ferroelectric III_2-VI_3 film and biaxial strain. *Phys. Rev. B* **101**, 184426 (2020).
41. Wang, D.-s, Wu, R. & Freeman, A. J. First-principles theory of surface magnetocrystalline anisotropy and the diatomic-pair model. *Phys. Rev. B* **47**, 14932–14947 (1993).
42. Yang, B. S. et al. Strain induced enhancement of perpendicular magnetic anisotropy in Co/graphene and Co/BN heterostructures. *Phys. Rev. B* **95**, 174424 (2017).
43. Wang, W. et al. Tunning magnetism and anisotropy by ferroelectric polarization in 2D van der Waals multiferroic heterostructures. *Mater. Today Phys.* **27**, 100803 (2022).
44. Zhang, J., Yang, B., Zheng, H., Han, X. & Yan, Y. Large magnetic anisotropy and strain induced enhancement of magnetic anisotropy in monolayer $TaTe_2$. *Phys. Chem. Chem. Phys.* **19**, 24341–24347 (2017).
45. Kresse, G. & Hafner, J. Ab initio molecular dynamics for liquid metals. *Phys. Rev. B* **47**, 558–561 (1993).
46. Kresse, G. & Furthmüller, J. Efficient iterative schemes for ab initio total-energy calculations using a plane-wave basis set. *Phys. Rev. B* **54**, 11169–11186 (1996).
47. Blöchl, P. E. Projector augmented-wave method. *Phys. Rev. B* **50**, 17953–17979 (1994).
48. Kresse, G. & Joubert, D. From ultrasoft pseudopotentials to the projector augmented-wave method. *Phys. Rev. B* **59**, 1758–1775 (1999).
49. Perdew, J. P., Burke, K. & Ernzerhof, M. Generalized Gradient Approximation Made Simple. *Phys. Rev. Lett.* **77**, 3865–3868 (1996).
50. Dudarev, S. L., Botton, G. A., Savrasov, S. Y., Humphreys, C. J. & Sutton, A. P. Electron-energy-loss spectra and the structural stability of nickel oxide: An LSDA +U study. *Phys. Rev. B* **57**, 1505–1509 (1998).
51. Grimme, S., Antony, J., Ehrlich, S. & Krieg, H. A consistent and accurate ab initio parametrization of density functional dispersion correction (DFT-D) for the 94 elements H-Pu. *J. Chem. Phys.* **132**, 154104 (2010).
52. Grimme, S., Ehrlich, S. & Goerigk, L. Effect of the damping function in dispersion corrected density functional theory. *J. Comput. Chem.* **32**, 1456–1465 (2011).
53. Grimme, S. Semiempirical GGA-type density functional constructed with a long-range dispersion correction. *J. Comput. Chem.* **27**, 1787–1799 (2006).
54. Thonhauser, T. et al. Van der Waals density functional: Self-consistent potential and the nature of the van der Waals bond. *Phys. Rev. B* **76**, 125112 (2007).
55. Henkelman, G., Uberuaga, B. P. & Jónsson, H. A climbing image nudged elastic band method for finding saddle points and minimum energy paths. *J. Chem. Phys.* **113**, 9901–9904 (2000).
56. Sheppard, D., Xiao, P., Chemelewski, W., Johnson, D. D. & Henkelman, G. A generalized solid-state nudged elastic band method. *J. Chem. Phys.* **136**, 074103 (2012).
57. Togo, A. & Tanaka, I. First principles phonon calculations in materials science. *Scr. Mater.* **108**, 1–5 (2015).

ACKNOWLEDGEMENTS

This work was supported by the National Natural Science Foundation of China (Grant No. 12004137), the Taishan Scholar Program of Shandong Province (Grant No. ts20190939), the Natural Science Foundation of Shandong Province (Grant Nos. ZR2020QA052 and ZR2020ZD35) and the Young Scholars Program of Shandong University (No. 2018WLJH65).

AUTHOR CONTRIBUTIONS

Y.W.: Formal analysis, investigation, visualization, data curation, writing—original draft. S.L.: conceptualization, methodology, supervision, investigation, data curation, writing—original draft and review and editing. Y.L.: supervision, project administration, funding acquisition. X.Z.: validation, supervision. X.X.: validation, supervision. W.J.: software, data curation.

COMPETING INTERESTS

The authors declare no competing interests.

ADDITIONAL INFORMATION

Supplementary information The online version contains supplementary material available at https://doi.org/10.1038/s41524-023-01178-2.

Correspondence and requests for materials should be addressed to Shengshi Li, Yanlu Li or Xian Zhao.